Data-driven characterization of thermal models for powder-bed-fusion additive manufacturing

Wentao Yan[a,c,e], Yan Lu[b], Kevontrez Jones[c], Zhuo Yang[d], Jason Fox[b], Paul Witherell[b], Gregory Wagner[c], Wing Kam Liu[c,e]

[a] *Currently at Department of Mechanical Engineering, National University of Singapore, 117575, Singapore*

[b] *Engineering Laboratory, National Institute of Standards and Technology (NIST), Gaithersburg, MD 20899, United States* [1]

[c] *Department of Mechanical Engineering, Northwestern University, Evanston, IL 60201, United States*

[d] *Department of Mechanical Engineering, University of Massachusetts Amherst, Amherst, MA 01003, United States*

[e] *Corresponding authors: mpeyanw@nus.edu.sg, w-liu@northwestern.edu*

Abstract

Computational modeling for additive manufacturing has proven to be a powerful tool to understand physical mechanisms, predict fabrication quality, and guide design and optimization. Varieties of models have been developed with different assumptions and purposes, and these models are sometimes difficult to choose from, especially for end-users, due to the lack of quantitative comparison and standardization. Thus, this study is focused on quantifying model uncertainty due to the modeling assumptions, and evaluating differences based on whether or not selected physical factors are incorporated. Multiple models with different assumptions, including a high-fidelity thermal-fluid flow model resolving individual powder particles, a low-fidelity heat transfer model simplifying the powder bed as a continuum material, and a semi-analytical thermal model using a point heat source model, were run with a variety of manufacturing process parameters. Experiments were

[1] The full descriptions of the procedures used in this paper may require the identification of certain commercial products. The inclusion of such information should in no way be construed as indicating that such products are endorsed by NIST or are recommended by NIST or that they are necessarily the best materials, instruments, software or suppliers for described purposes.

performed on the National Institute of Standards and Technology (NIST) Additive Manufacturing Metrology Testbed (AMMT) to validate the models. A data analytics-based methodology was utilized to characterize the models to estimate the error distribution. The cross comparison of the simulation results reveals the remarkable influence of fluid flow, while the significance of the powder layer varies across different models. This study aims to provide guidance on model selection and corresponding accuracy, and more importantly facilitate the development of AM models.

Keywords: Model characterization, Computational model, Modeling assumption, Powder bed, Additive manufacturing

---

1. Introduction

Powder bed fusion additive manufacturing (AM) technologies for metallic components, such as electron beam melting (EBM) and laser powder bed fusion (L-PBF), are promising in manufacturing components with complex geometry [1] and manipulating chemical compositions and mechanical properties [2, 3, 4]. Computational modeling has proven to be a powerful tool to help understand physical mechanisms, predict fabrication quality, and guide design and optimization. Various models have been developed with different assumptions and purposes. For the meso-scale models of molten pool and heat transfer, depending on the level of simplification of the powder bed geometry and physics, there are three main types:

1. High-fidelity computational fluid dynamics (CFD) models that resolve the thermal-fluid flow behaviors of individual powder particles. Examples are those developed by Körner et al. [5] using their in-house code based on the Lattice Boltzmann Method, by Lawrence Livermore National Lab [6, 7] using their in-house code ALE3D, by Qiu et al. [8] using the open-source code OpenFOAM, and by the current authors [9, 10] using the software FLOW-3D. The computation time of these models can be extremely high, up to thousands of central processing unit (CPU) hours, thus the simulation domain is usually limited to one or a small number of short tracks, with the domain size at most a few millimeters in each dimension, while the corresponding physical time is on the order of milliseconds. Note that there are some continuum-based CFD models [11] that simplify powder bed as a continuum layer

but neglect the recoil pressure and capillary forces. Such type of model is not included in this study, because it is not so widely used.

2. Continuum-based thermal models that simplify the powder bed as a continuum material (different from that of the substrate and condensed layers), and incorporating heat transfer but not fluid flow [12, 13, 14, 15]. Most existing finite element method (FEM) software packages, e.g., ABAQUS and ANSYS, are capable of such simulations. The computation is less expensive and can enable part scale simulations, e.g., tens to hundreds of CPU hours for a small component (a few centimeters in each dimension). However, the simulation cost can still increase quickly with the dimension of the simulation domain.
3. Semi-analytical thermal-conduction models that only consider the thermal conduction in a homogeneous continuum, such as the isotherm migration model using a point heat source model [16, 17]. These models can only estimate the steady-state temperature field in single track cases. The calculation can be done typically in Matlab within seconds.

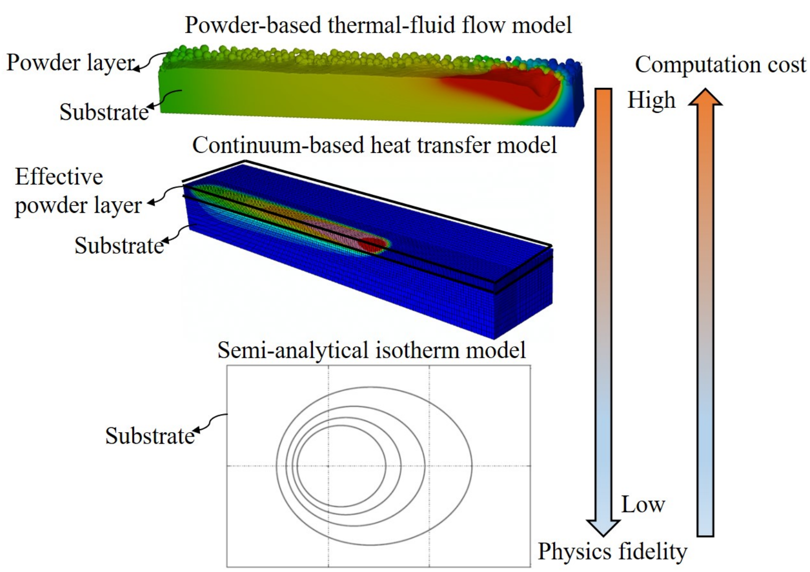

Figure 1: Computational models for powder bed AM: from high-fidelity to low-fidelity.

When implementing or leveraging models, various models have pros and cons depending on user objectives. However, despite differences in computational cost and accessibility, these models are still difficult to choose from, especially for end-users, because there is a lack of quantitative comparison and standardization [18, 19, 20].

In this work, we conduct a variety of simulations to quantify solution differences due to model assumptions and to assess the importance of several key physical factors, which can provide guidance for the development and selection of models for specific purposes. These models are introduced in Section 2, from the high-fidelity, powder-based thermal-fluid flow models, to the low-fidelity, continuum-based thermal models, to the simplest semi-analytical models based on the point heat source model. Section 3 presents the experimental methods. In Section 4, simulation results are compared and uncertainty is discussed. A data analytics-based approach is utilized to characterize the models and estimate the error distributions in Section 5. Finally, a brief summary is given in Section 6.

2. Models

2.1. Model characteristics

The three types of models (① powder-scale thermal-fluid flow model [9, 10, 21], ② continuum thermal model [12, 13, 14, 22, 23], and ③ semi-analytical model [16, 17]) are schematically shown in Fig. 2. While the powder-scale thermal-fluid flow model and continuum thermal model are commonly seen, the semi-analytical model, particularly the so-called isotherm migration model used in this study, is less common. The basis of this isotherm migration model is the steady-state solution (Eq.2) of the heat conduction problem (Eq.1), where a point heat source is applied to a semi-infinite work-piece moving at a constant speed U along the X direction. Equations are given as [16, 17]:

$$c_p\rho(\frac{\partial T}{\partial t} + U\frac{\partial T}{\partial x}) = k(\frac{\partial^2 T}{\partial x^2} + \frac{\partial^2 T}{\partial y^2} + \frac{\partial^2 T}{\partial z^2}) + q(x) \tag{1}$$

$$T(x,y,z) = T_0 + \frac{p}{2\pi k\sqrt{x^2+y^2+z^2}} \exp\frac{x - \sqrt{x^2+y^2+z^2}}{2k/(\rho c_p U)} \tag{2}$$

where T_0 is the initial temperature, $q(x)$ is the moving heat source, p is the laser power, and k, ρ and c_p are the thermal conductivity, density and specific heat of the material as listed in Table 1.

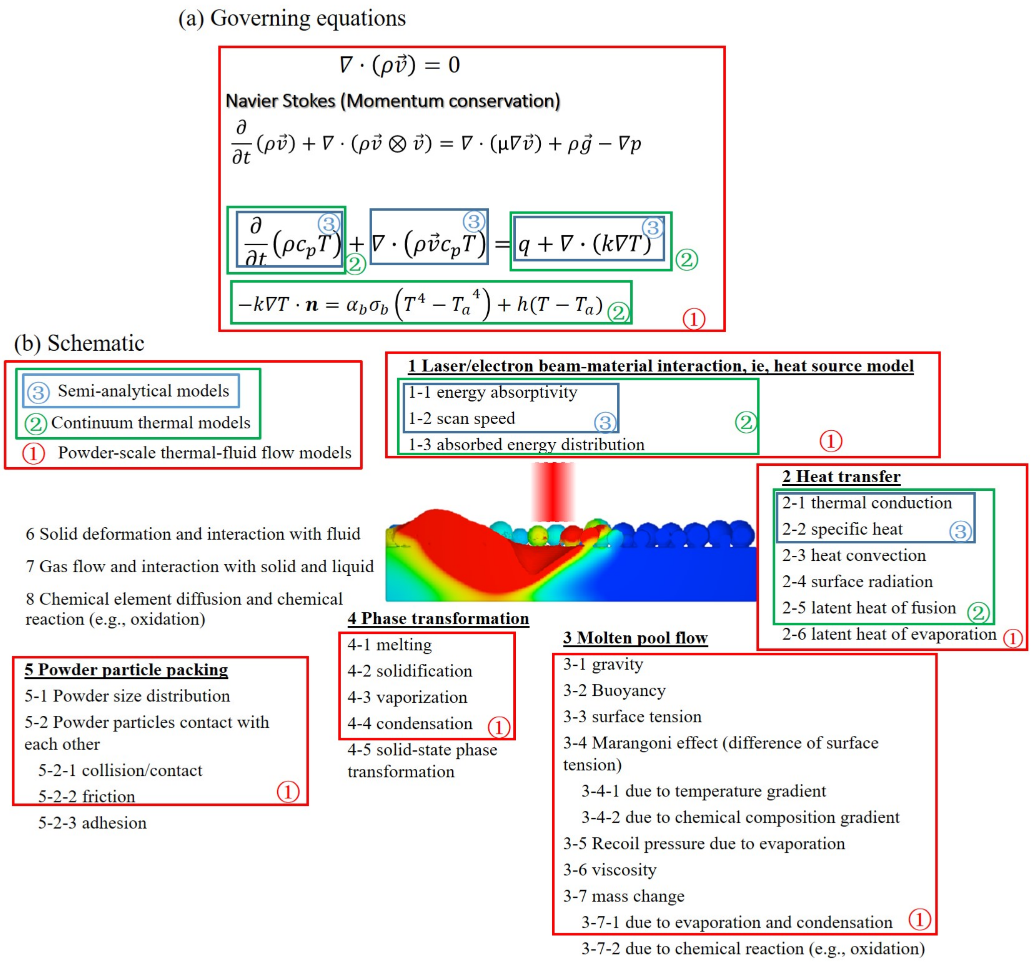

Figure 2: Physical factors incorporated in models (① powder-scale thermal-fluid flow model, ② continuum thermal model, and ③ semi-analytical model): (a) incorporated terms in the governing equations, (b) schematic. The incorporated factors in each model are inside the corresponding boxes with the model label, while the factors outside the labeled box are not incorporated in the corresponding model. There are some factors that have not been incorporated by any of the models.

From the high-fidelity model to the low-fidelity model, there is a progressive order reduction, as schematically shown in Fig. 3. The high-fidelity powder-scale thermal-fluid flow model is considered to be able to capture major physical factors and to reproduce the experiments relatively well. The order reductions from the CFD model to the FEM thermal model include the simplifications of the powder bed geometry, multi-reflection of laser and molten pool flow physics, in particular the neglect of Marangoni effect, and evaporation and the resultant recoil pressure. The reduced orders from the FEM thermal model to the semi-analytical model include the neglect of the effective powder layer, heat source diameter and heat loss. In other words, the semi-analytical simulations are very close to the FEM thermal simulations of a very narrow laser heating a bare plate with de-activated (or negligible) latent heat and heat loss. Consequently, the material parameters required in each model vary, as listed in Table 1 (the material used in this paper is nickel alloy Inconel 625, or IN 625).

Table 1: Material (IN 625) parameters used in the models

Parameter	Value	Model
Solidus temperature T_s	1563 K [24]	①②
Liquidus temperature T_l	1623 K [24]	①②③
Density ρ	8440 kg/m^3 [25]	①②③
Latent Heat of fusion L	2.72×10^5 J/kg [26]	①②
Latent heat of evaporation (L_v)	9.7×10^6 J/kg	①
Saturated vapor pressure (P_{s0})	1.013×10^5 Pa at 3315 K	①
Specific heat (c$_p$)	temperature-dependent [25]	①②③
Thermal conductivity (k)	temperature-dependent [25]	①②③
Surface radiation coefficient (α_b)	0.4	①②
Surface tension coefficient (σ)	1.68 N/m	①
Marangoni coefficient ($\sigma_s^T = \frac{\Delta\sigma}{\Delta T}$)	2.6×10^{-4} N/(m·K)	①
Viscosity (μ)	0.005 Pa·s	①

On the other hand, incorporating more physical phenomena introduces more degrees of freedom, more complex equations, and thus higher computational cost. For each simulation case of a single track (2-3 mm long) in this study, the computational cost of the thermal-fluid flow model is about 100 hours on a common desktop, and that of the FEM thermal model implemented into an in-house code developed at Northwestern University [22, 23] is about 3 minutes, while that of the semi-analytical model calculated using Matlab is less than 30 seconds. Thus, although the high-fidelity thermal-fluid flow model more accurately captures the influence of most physical mechanisms, only a limited number of these expensive high-fidelity simulations were conducted.

It should be mentioned that the mesh size and computational method are usually different for different models; however, mesh convergence tests for each model have been performed to ensure that mesh size error is negligible compared to differences between models, and each computational method has been verified against some classical benchmark tests to ensure that the equations are solved accurately. That is, to assess the influence of the modeling assumptions, a fair comparison of the simulation results is required to exclude the numerical error of each model, which is achieved with the optimal mesh size and time step size for each model, instead of the same mesh size and time step size. Specifically, the mesh size and time step size are 4 μm and 4×10^{-8} s for the thermal-fluid model, and 10 μm and 1×10^{-6} s for the FEM thermal model, while there are 10 isotherms in the semi-analytical model.

2.2. Design of experiments

Nine sets of manufacturing parameters are selected, as listed in Table 2. These sets of parameters are representative of all the four regimes of the molten pool behaviors: balling effect, thermal-conduction mode, transition mode and keyhole mode.

Table 2: Fabrication parameters

Laser power p (W)	Scan speed v (m/s)	Line energy density p/v (J/cm)	mode
195	0.80	2.4	thermal-conduction
195	0.50	3.9	transition
195	0.20	9.8	keyhole
122	0.80	1.5	thermal-conduction
122	0.50	2.4	thermal-conduction
122	0.20	6.1	transition
49	0.80	0.61	balling
49	0.50	0.98	thermal-conduction
49	0.20	2.5	thermal-conduction

In principle, models incorporating more physical phenomena have higher prediction accuracy. However, the neglect of two or more physical factors in some cases may counteract each other, thereby achieving good accuracy serendipitously. With this in mind, in addition to evaluating the accuracy of the three models, we try to assess the individual influence of several major physical factors. Several groups of simulations for each model with varied settings were conducted (see Fig. 3):

1. **Control groups: CFD simulations containing powder bed ("CFD-powder" in Fig. 3); FEM thermal simulations with effective powder bed ("FEM-powder" in Fig. 3); semi-analytical calculation with bulk material properties ("ISO-plate" in Fig. 3).** These three groups of simulations are typically used for predictions, and thus can be used to evaluate accuracy against the powder bed experiments.
2. **Comparison groups: CFD simulations without powder bed ("CFD-plate" in Fig. 3); FEM thermal simulations of a bare plate ("FEM-plate" in Fig. 3); semi-analytical calculation with effective powder bed properties ("ISO-powder" in Fig. 3).** These three groups of simulations are rarely used in practice, and the purpose here is for comparison with the control groups. Through direct comparison, the influence of the powder layer in each model can be assessed. Additionally, cross-comparison of the simulation results can shed light on the individual influence of the major physical factors, based on the discussion of model order reduction in Section 2.1. For instance, the comparison between the CFD and FEM thermal simulations indicates the influence of molten pool flow, and the difference between the FEM thermal and semi-analytical simulations can partially reveal the influence of the laser heat source model.

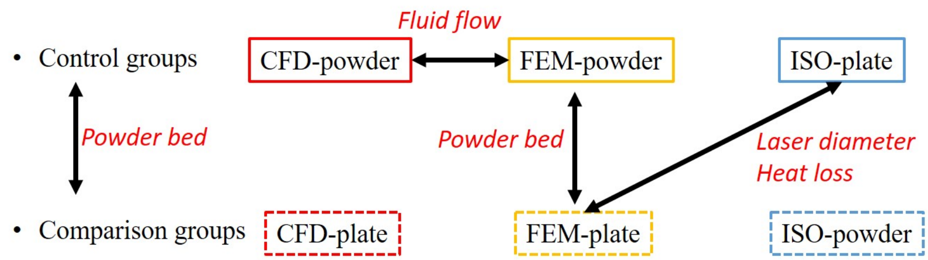

Figure 3: Control and comparison groups of simulations. The arrows and associated text indicate the major differences between the linked models. The major difference between the control and comparison groups is the incorporation and neglect of the powder bed. The cross-comparison between the CFD-powder and FEM-powder simulation results can reveal the influence of molten fluid flow, and that between the FEM-plate and ISO-plate simulation results reveals the influence of laser diameter and heat loss. ISO-plate and ISO-powder simulations refer to the semi-analytical simulations using the properties of a dense plate and loose powder bed, respectively.

The selected key performance indicators (KPIs) are molten pool dimensions, including width, depth and length, which have remarkable influence over the fabrication quality. However, in the experiments, only ex-situ analysis of the laser scan tracks was performed, while in-situ monitoring of the melting process was challenging. In this manuscript, only molten pool width from experiments was obtained. While we did not measure the molten pool depth for validation, we validated the thermal-fluid flow model's prediction of molten pool depth against high-speed X-ray imaging experiments at Argonne National Lab in the previous work [27].

3. Experiments

Single track experiments were performed using the Additive Manufacturing Metrology Testbed (AMMT) prototyping system at National Institute of Standards and Technology (NIST) [28]. The powder material is nickel alloy 625 (IN 625), and powder diameter distribution follows a Gaussian distribution function with d10=14 μm, d50=28 μm, and d80=43 μm[2]. The actual layer thickness at steady state is 40 μm, and the laser diameter is D86=100 μm. Investigation of experimental results found that experiments

[2]The d10/d50/d80 is the diameter at which 10%/50%/80% of the sample's mass is composed of particles with a diameter less than the value

at a power of 49 W produced unreliable data, since the laser power output was not reliable below 49 W, and for this reason these measurements were ignored. Nevertheless, the simulation results for these cases are retained to enrich the comparison of models, given that the models are considered to be able to provide reasonable predictions for these cases after being validated by other experimental cases. Ex-situ analysis of the laser scan tracks from the experiment was performed via optical microscope for measurement of the scan track width. In order to better assess the molten pool width, a detailed record of the width along a 1 mm long section at the center of each scan track was obtained by manually tracing the track edges, and the average molten pool width and its standard deviation were calculated using the commercial software Matlab. More details about the methodology can be found in [29]. A similar measurement methodology was also applied for CFD simulation results (see Fig.4), so that both the mean value and standard deviation of the simulated molten pool width were obtained. Note that neither the FEM thermal simulation results nor the semi-analytical calculation results have fluctuations in width because of the assumption of homogeneity and the neglect of laser multi-reflection and temperature-dependent surface tension.

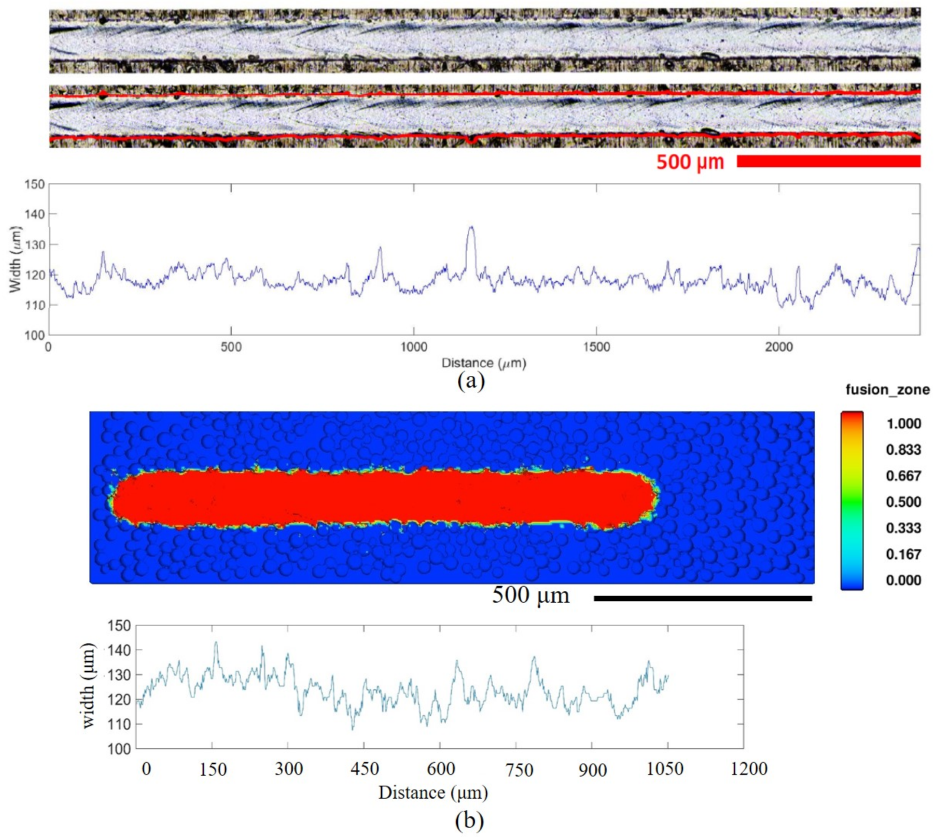

Figure 4: Examples of measuring track width: (a) an experimental sample [29] and (b) a CFD simulation result. In this case, the laser power is 122 W, and scan speed is 0.5 m/s.

4. Results and discussion

Single tracks on the first powder layer with a thickness of 40 μm were manufactured in experiments and also simulated using the three different control group models. The simulation and experimental results are summarized in Table 3, including the relative difference $|\frac{width_{simulated}-width_{experimental}}{width_{experimental}}|$. It is noted that the balling effect occurred in the experiment for the case 122 W-0.8 m/s while it did not in the corresponding three simulations. One large source of experimental uncertainty that may contribute to this discrepancy is the powder particle packing and accuracy of the experimental layer thickness. It is very difficult to ensure the first powder layer thickness to be exactly 40 μm in the experiments, while any powder particles above the 40 μm thickness are removed in the simulation. As a result, the powder particle packing in the simulation usually underestimates the packing density of such a thin powder layer, leading to a lower possibility of balling in the simulation.

Table 3: Simulated molten pool dimensions and experimentally measured melt width

	Simulated length/depth/width [μm] and relative difference			
Cases	CFD	FEM thermal	semi-analytical	Experiment
	500	528	151	
195W-0.8m/s	89	50	52	
	117±7 (11.3%)	141 (6.8%)	104 (21.2%)	132±14.1
	491	482	155	
195W-0.5m/s	111	62	65	
	137±8 (8.5%)	176 (10.9%)	130 (13.2%)	149.7±7.3
	489	439	171	
195W-0.2m/s	152	91	99	
	216±6 (4.9%)	241 (16.9%)	198 (3.9%)	206±20.9
	335	401	97	
122W-0.8m/s	70	40	40	balling
	102±5	121	80	
	302	356	101	
122W-0.5m/s	85	50	50	
	122±6 (3.9%)	141 (11.1%)	100 (21.2%)	126.9±17.0
	319	330	114	
122W-0.2m/s	88	73	76	
	170±7 (13.2%)	201 (33.8%)	152 (1.2%)	150.2±8.2
	122	328	43	
49W-0.8m/s	40	31	25	
	62±9	81	50	
	159	233	46	
49W-0.5m/s	57	31	30	
	84±7	51	60	
	155	187	54	
49W-0.2m/s	66	43	44	
	121±5	140	88	

4.1. Differences due to the neglect of molten pool flow

4.1.1. Molten pool width

Based on comparison of the molten pool width (Fig. 5), the CFD model has the highest prediction accuracy: the relative differences of the mean values are all within 15% and mostly within 10%, while there are overlaps if accounting the standard deviation. The FEM thermal model shows that the prediction error is below 20% for most of the cases, except that it is about 30% for the case 122 W-0.2 m/s. The semi-analytical model shows a prediction error below 30%. Neither the FEM thermal models nor the semi-analytical model explicitly incorporate the molten pool flow, which could be a major source of prediction errors.

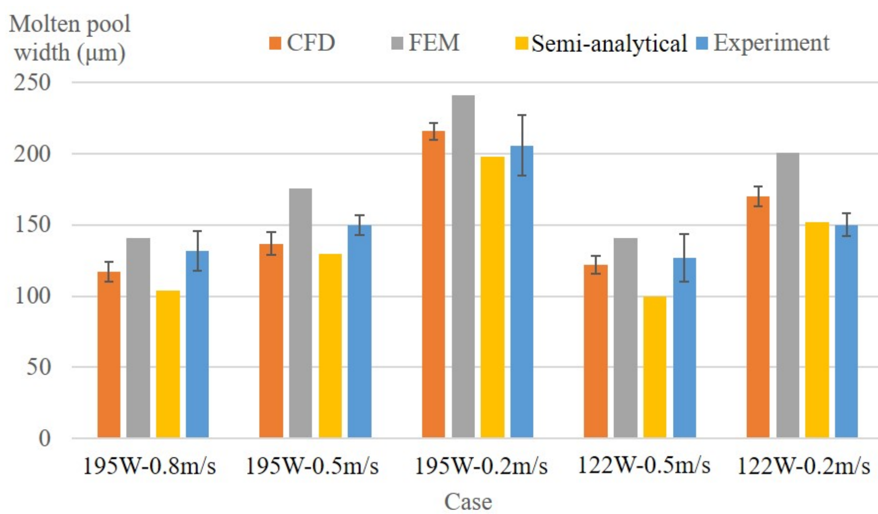

Figure 5: Molten pool width by experiments and the three models at different cases. For experiments and CFD model, the error bars represent the standard deviations of the molten pool width. Neither the FEM thermal model nor the semi-analytical model has fluctuations in width because of the assumption of homogeneity.

The FEM thermal models use an effective continuum material layer to implicitly represent the powder layer and incorporate the thermal conduction, surface radiation and convection; therefore, the FEM thermal models can achieve good accuracy in the thermal-conduction mode, in particular with intentionally enhanced thermal conductivity in the molten liquid state to incorporate the enhanced heat transfer by the molten pool flow [30]. However, in the keyhole mode, the recoil pressure becomes dominant in the molten pool flow and thereby dramatically changes the molten pool shape and dimensions, which are rather different from those in the thermal-conduction model; consequently, the prediction accuracy of the FEM thermal models reduces remarkably (see the molten pool width for cases 122 W-0.2 m/s and 195 W-0.2 m/s). More specifically, the FEM models usually overestimate the molten pool width, because the neglect of the molten pool flow especially in the keyhole mode leads to less heat dissipation in depth and thus more residual heat within the powder layer to widen the molten pool width in the horizontal direction.

The semi-analytical model typically underestimates the molten pool width. In the semi-analytical model, neither the powder layer nor the molten pool flow is incorporated; that is, the problem is idealized as a simple thermal conduction problem with a point heat source heating a substrate. The point heat source model ignores the distributed input energy within the finite laser diameter, thereby underestimating the molten pool width. Since the dense substrate has a much higher thermal conductivity than the loose powder layer, the input heat disperses more quickly in each direction, expanding the molten pool width. These two factors counteract each other to some extent. In particular, in the cases 122 W-0.2 m/s and 195 W-0.2 m/s, which are in the keyhole mode, the calculated molten pool width of the semi-analytical model shows very good agreement with experiments. However, this might not always be true for other cases in the keyhole mode.

Based on the discussion above, we can conclude that because of varying contributions of the different mechanisms of molten pool formation in the thermal conduction and keyhole modes, it is difficult, if not impossible, to tailor FEM thermal models to be accurate in both modes. One approach could be to adjust the laser heat source model at different input powers, for example, the rotational Gaussian body flux model (nail-shaped) for the keyhole mode, and the surface flux or the Goldak body flux model for the thermal conduction mode; however, this approach not only lacks rigorous physical foundation, but also requires experimental calibration [12].

4.1.2. Molten pool length

As no experimental data was obtained for the molten pool length, the high-fidelity CFD simulations were used to benchmark the FEM and semi-analytical models. We validated this CFD model's prediction of molten pool length against high-speed X-ray imaging experiments at Argonne National

Lab [27], and the relative difference was within 10%; thus the high-fidelity CFD simulations are deemed to have sufficient accuracy.

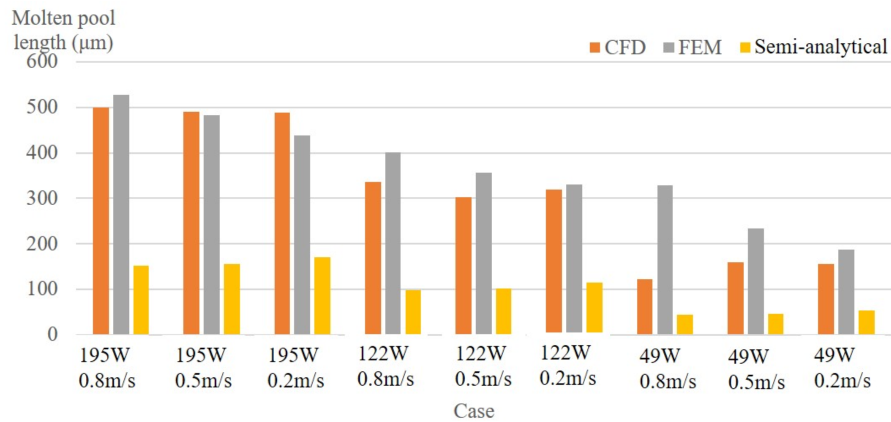

Figure 6: Molten pool length by the three models at difference cases.

The FEM thermal model predicts the molten pool length within 20% from the CFD predictions (Fig. 6), except the cases of 49 W-0.8 m/s and 49 W-0.5 m/s. For those two cases, the FEM-simulated molten pool depths (31 μm, see Table 3) are smaller than the powder layer thickness so that the heat in the molten pool cannot be conducted away through the substrate, thereby enlarging molten pool length; on the other hand, the CFD-simulated molten pools reach the substrate. This can explain why at the laser power of 49 W, the FEM-simulated length decreases with the decrease of scan speed while the CFD-simulated length increases. The prediction accuracy of molten pool length is at the same level as that of molten pool width. In contrast, the predicted molten pool length from the semi-analytical model with either bulk material properties or effective powder bed properties is much smaller than the CFD-predicted value. In the semi-analytical model with bulk material properties, the dense substrate has much higher thermal conductivity than that of a loose powder bed, and thus disperses heat too quickly to maintain a long molten pool as within a powder bed , while in the semi-analytical model with effective powder bed properties, the thermal conductivity is too low to disperse heat to enlarge the molten pool. Additionally, the point heat source model does not account for the diameter of the laser beam. Therefore, it can be concluded that the semi-analytical model lacks fidelity to accurately predict the molten pool length in powder bed fusion processes.

4.2. Differences due to the neglect of powder bed

Direct comparison between the Control and Comparison groups reveals the influence of the powder layer. The high-fidelity CFD simulations of single tracks on a substrate, in comparison with the powder bed cases, are shown in Fig. 7. Without a powder layer, the molten pool width is 108±4 for the 195 W-0.8 m/s case and 131±3 for the 195 W-0.5 m/s case, while it is 117±7 and 137±8 with the 40 μm thick powder layer for those two cases, respectively. The difference due to the powder layer is within 10%. Since the mean diameter of the powder particles is close to the layer thickness, in most locations there is only one powder particle in the vertical direction of the powder layer. Thus the influence of the powder bed characterization is marginalized.

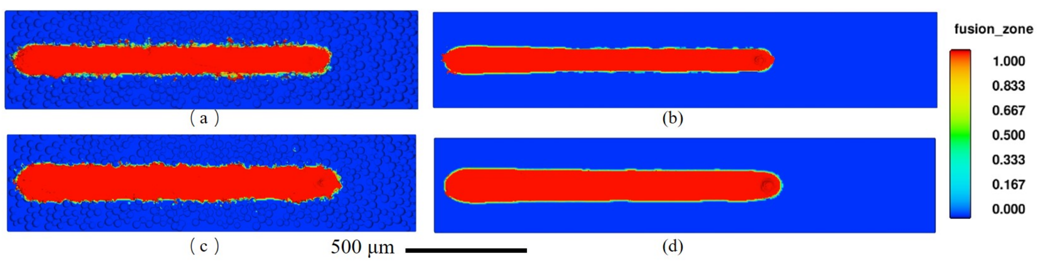

Figure 7: High-fidelity CFD simulation results of single tracks: 195 W-0.8 m/s on (a) a powder bed and (b) a flat substrate; and 195 W-0.5 m/s on (c) a powder bed and (d) a flat substrate.

In the FEM thermal model, the powder bed is implicitly incorporated by assigning effective material properties to the continuum. To assess the influence of the powder bed, simulations were also conducted without the effective powder layer, i.e., a laser scanning a bare plate. As shown in Table 4, the powder bed makes a remarkable difference ($|\frac{dimension_{bareplate} - dimension_{powderbed}}{dimension_{powderbed}}|$): the molten pool width values of the bare plate cases are about 30% smaller than those of the powder bed cases, and the depth values are mostly 10%-20% smaller, while the length values show a larger fluctuation.

In the semi-analytical model, the material possesses uniform material properties. That is, the semi-analytical model cannot incorporate the powder bed and substrate at the same time. Assigning the continuum material with the relatively high thermal conductivity of the bulk material or the relatively low thermal conductivity of the loose powder bed, makes a large difference in the simulation results, as shown in Table 4, where the relative differences for the semi-analytical calculations are $|\frac{dimension_{powderbed}-dimension_{bareplate}}{dimension_{bareplate}}|$. Based on the results and the discussion in Section 4.1.1, it is recommended that the semi-analytical model should use the thermal conductivity of the bulk material.

Moreover, the "NaN" in Table 4 indicates that the calculation in Matlab could not get a result with errors "matrix singularity", due to the low thermal conductivity of the powder layer (in this study, 1 W/(m·K) based on simulations [13] and experiments [31]). If the thermal conductivity of the powder layer is set as 3 W/(m·K), the calculated molten pool length, depth and width are 42, 18 and 36 [μm].

Table 4: Simulated molten pool dimensions by the FEM thermal and semi-analytical models with/without incorporating the powder bed: length/depth/width [μm] and the relative differences

	FEM thermal		semi-analytical	
Cases	bare plate	powder bed	bare plate	powder bed
195W-0.8m/s	358/44/100	528/50/141	151/52/104	39/23/46
	32.2%/12%/26.1%		72.3%/55.8%/55.8%	
195W-0.5m/s	358/56/120	482/62/176	155/65/130	43/29/58
	25.7%/9.8%/31.8%		74.2%/55.4%/55.4%	
195W-0.2m/s	358/85/177	439/91/241	171/99/198	55/44.5/89
	18.5%/6.6%/26.6%		67.8%/55.1%/55.1%	
122W-0.8m/s	238/32/82	401/40/121	97/40/80	19/17.5/35
	40.6%/20.0%/32.2%		70.1%/56.3%/56.3%	
122W-0.5m/s	243/42/97	356/50/141	101/50/100	30/22.5/45
	31.7%/16.0%/31.2%		69.3%/55.0%/55.0%	
122W-0.2m/s	257/77/140	330/73/201	114/76/152	40/34.5/69
	22.1%/5.5%/30.3%		64.9%/54.6%/54.6%	
49W-0.8m/s	109/17/58	328/31/81	43/25/50	NaN
	66.8%/45.2%/28.4%		NaN	
49W-0.5m/s	114/22/68	233/31/51	46/30/60	16/14/28
	51.1%/29.0%/33.3%		65.2%/53.3%/53.3%	
49W-0.2m/s	123/35/87	187/43/140	54/44/88	22/20.5/41
	34.2%/18.6%/37.93%		59.3%/51.1%/51.1%	

4.3. Differences due to heat loss

As discussed in the beginning of Section 2, the simplifications in going from the FEM thermal model (incorporating the powder bed) to the semi-analytical model include the neglect of the effective powder layer, heat source diameter, latent heat, and heat loss. Thus, the FEM thermal simulations of a bare plate are rather close to the semi-analytical calculations for a bare plate, with the differences coming from the treatment of the heat source diameter, latent heat, and heat loss. It is observed that the predictions of width and depth are rather close, but those of length are rather different.

The influence of the heat loss due to the surface radiation and convection, can be excluded as negligible for the cases of interest. This can be easily proved via theoretical approximation. It is assumed that the surface heat loss through radiation and convection is dominated by that from the molten pool surface area: the surface temperature is assumed 2000 K, the molten pool area is on the order of 10^{-7} m^2 (an ellipse pool with a length radius of 300 μm and a width radius of 100 μm, so the area is $\pi\times$ 300 μm $\times$ 100 μm); then the heat loss through surface radiation is calculated to be 5.67×10^{-8} W/(m$^2\cdot$ K^4)$\times$(2000 K)^4 $\times$ 10^{-7} m^2=0.09 W, and assuming the convective coefficient is 100 W/(m$^2\cdot$K), heat loss through surface convection is calculated to be 100 W/(m$^2\cdot$K)$\times$(2000 K - 300 K)$\times10^{-7}$ m^2=0.017 W. Therefore the heat loss due to surface radiation and convection is smaller than the input power by four orders of magnitude.

4.4. Differences due to the laser heat source model

It is of critical importance to specify the definition of the laser diameter along with the given value. For ideal single-mode Gaussian beams, there are four types of definitions that are commonly used:

- Full width at half maximum (FWHM): the diameter is the full width of the laser beam at half of its maximum intensity.
- D86 width (same value with $1/e^2$ width and D4σ): 86.5% (i.e., $1-1/e^2$) of the beam power is within this diameter.
- D95 width: 95% of the beam power is within this diameter.
- D99 width: 99% of the beam power is within this diameter.

The relationships between these definitions for a given Gaussian beam are

$$\begin{cases} \text{FWHM} = 0.5886 \cdot D86 \\ D95 = 1.23 \cdot D86 \\ D99 = 1.52 \cdot D86 \end{cases} \tag{3}$$

It is obvious that the misuse of the definition will make a notable difference in the prediction. The measurement uncertainty of the laser beam size will also lead to uncertainty in the model predictions. For instance, for the substrate melting cases of the thermal-fluid flow simulation, with the FWHM increasing from 45 μm to 50 μm, the relative increases of molten pool length and width are nearly 10% and 15%, while the relative decrease of depth is nearly 10%.

It is worth noting that molten pool width typically falls into a small range relative to the laser beam diameter when the laser power is moderate. The underlying reasons are 1) only a small area around the laser center can absorb enough laser power to get melted; 2) the molten pool expands rather slowly in the horizontal direction due to the low thermal conductivity of the powder bed; 3) most of the absorbed energy dissipates through the substrate with high thermal conductivity. In this regard, the point heat source model with a diameter of 0 used in the analytical semi-analytical model leads to remarkable underestimation of the molten pool width, which is counteracted in some extent by the high thermal conductivity of the dense substrate (see the discussion in Section 4.1.1). However, if the continuum material in the semi-analytical model uses the effective thermal conductivity of loose powder bed (10% of that of the bulk material), the underestimation of the simulated molten pool width will not be counteracted, as shown in Table 4.

The energy absorptivity is believed to be more significant, since it directly determines the actual power input. However, it is influenced by a number of factors, e.g., the wavelength and polarization of the laser, the material compositions, the local incidence angle in the complex surfaces (powder particles and molten pool surfaces), and multiple reflections. This issue requires extensive and systematic studies, which are not included in the current work.

4.5. Model selection guidance

As discussed above, the high-fidelity CFD model shows the highest accuracy (10% deviation in molten pool dimension predictions), and the FEM thermal model shows 20% deviation, while the semi-analytical model shows

30% deviation in molten pool width but does not accurately predict molten pool length. As trade-offs, higher fidelity models not only take more computation time, but also require many additional parameter considerations and information that may not always be readily available. In such cases, it is useful to know what modeling approach is most suitable for the parameters available, what the relative uncertainty may be, and which additional parameters may help in developing a higher fidelity model.

The incorporation of fluid flow could make a difference of 20% in the molten pool dimension prediction, particularly considering the different dominant mechanisms in the thermal-conduction and keyhole modes. To accurately model the molten pool flow, the additional parameters of importance include (as listed in Table 1): viscosity, temperature-dependent surface tension coefficient, and the evaporation rate and recoil pressure which are closely related to the local temperature and chemical compositions as well as the ambient pressure [32]. In particular, several different equations for the evaporation rate and recoil pressure were used in different models [32, 6, 8], and the solution variability caused by choosing different models is worth quantifying in the future.

The incorporation of powder layer can lead to a significant difference up to 30% in the FEM thermal simulations. In contrast, in the CFD simulations, the influence is relatively small ($< 10\%$), especially in the keyhole mode, which has also been demonstrated by the high-speed X-ray imaging performed at Argonne National Lab [33].

A 10% uncertainty in laser diameter can lead to a difference of 10% in the CFD simulations. More importantly, failure to employ a definition of laser spot diameter that is consistent with the experiment may lead to a significant difference in results.

According to the theoretical analysis, the heat loss due to the surface convection and radiation can be neglected. Thus, the convective coefficient and emissivity are not of high priority for the models, though the emissivity is critical in interpreting infrared measurement of the manufacturing process.

5. Data-Driven Model Characterization for Error Mapping

This section aims to provide an example guideline of model usage by analyzing the global and local model performance based on the limited volume of data on molten pool width. Data-driven model characterization has the capability to provide insight into error maps. The objective is to provide error distribution maps (see Fig. 8) that aid selection of the most appropriate model, given a set of usage conditions by the end-user. Note that the result shown in this section is based on the 5 data points from Table 4. The sample size is relatively inadequate to provide a consolidated conclusion. However, this section aims to provide a demonstration of the general methodology. The error map accuracy could be improved in the future by adding more experimental measurements and simulated results.

Fig. 8 shows the predictive error distribution of the CFD, FEM thermal, and semi-analytical models. It uses a triangulation-based natural neighbor interpolation method to map the error distribution based on the difference between simulation and the experimental results [34]. The colormap indicates the scale of the relative error ($|\frac{\tilde{y}_i - y_i}{y_i}|$) from 0 (dark blue) to 0.3 (yellow). The experiment observes the balling at line energy density equal to 152.5 J/m and the closest successful measurement is located at 244 J/m (122 W-0.5 m/s) and 243.75 J/m (195 W-0.8 m/s). The surrogate model assumes the region of the parameter space that has line energy density less than 243.75 J/m may display balling. As a result, the top triangular area is marked as balling even though the simulation model can make a calculation in this domain. The figure marks the relative error of molten pool width between prediction and experimental results on the five measurement points.

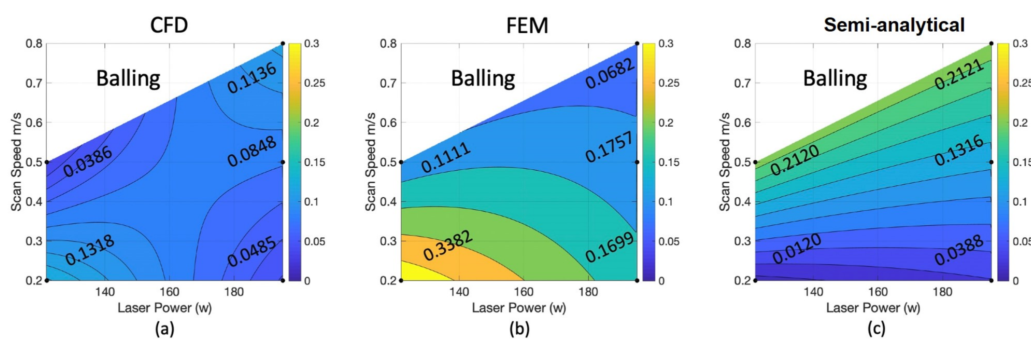

Figure 8: Error distribution maps for (a) CFD, (b) FEM thermal, and (c) semi-analytical models. These are only based on the five data points on molten pool width.

As mentioned in previous sections, the global model performance can also be observed through the error distribution maps. Each model gives superior performance in a different part of the parameter space. Fig. 9 shows the model-domain map for CFD, FEM thermal, and semi-analytical models. Each colored domain indicates the model that can provide the lowest predictive error. The CFD model dominates the area with moderate scan speed. The FEM model is more sensitive to high speed and high power domain. The semi-analytical model mainly dominates the area with low scan speed. It should be noted that the results (especially on the semi-analytical model) are purely based on the limited volume of data points on molten pool width, and thus can neither be applicable to molten pool length/depth nor be very accurate. An end-user can refer to such maps to select the model based on their design. The accuracy of the presented maps is dependent on the data presented here, and can be enhanced by increasing the volume and accuracy of data.

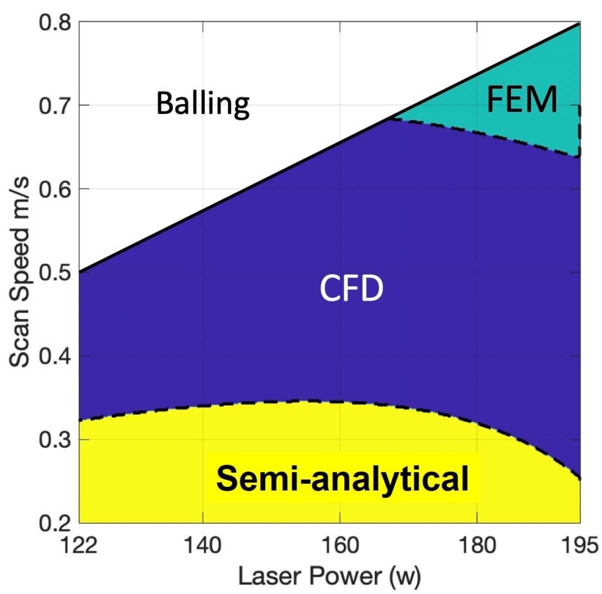

Figure 9: Model-domain map on prediction of molten pool width based on the limited volume of data. Green domain is dominated by FEM. Blue domain is for CFD model. Yellow domain is for semi-analytical model. The white area is the balling domain caused by low energy density.

Table 5 lists the characteristics of CFD, FEM, and semi-analytical models deduced from the error distribution map, based on the current sample size. End-users can choose the most appropriate model using this conceptual “cheat sheet” that characterizes the behavior of different simulation and surrogate models. End-users can make decisions based on the design properties and requirement on accuracy and efficiency. For example, the CFD model can provide the most accurate prediction for moderate scan speed when computational efficiency is not the first priority.

Table 5: Characteristics of CFD, FEM, and semi-analytical models

Model	Global Accuracy	Cost	Dominated Domain
CFD	High	High	Moderate scan speed
FEM	Medium	Medium	High power high scan speed
Semi-analytical	Low	Low	Low scan speed

6. Summary

In this study, a set of CFD, FEM and semi-analytical models with varied assumptions were run to characterize the molten pool models based on model performance, and to assess the reduction in accuracy due to each assumption. For the given sets of manufacturing parameters, the thermal-fluid flow model showed the highest prediction accuracy (relative error $< 10\%$) of molten pool width,the FEM thermal model possessed medium accuracy (relative error $< 20\%$), while the semi-analytical model showed the lowest accuracy (relative error $< 30\%$). The uncertainty due to the neglect of molten fluid flow can be significant (20% or more), while the influence of surface convection and radiation is minor. The neglect of the powder layer or uncertainty of laser diameter can also lead to an error of 10% for the thermal-fluid flow model, while for the FEM and semi-analytical simulations multiple simplifications can either counteract or enhance the errors. A couple of other significant error sources, including energy absorptivity in the heat source model and self-consistent evaporation and recoil pressure (i.e., mass loss, energy loss and momentum conservation), are worth extensive and systematic studies in the future.

Data-driven model characterization provides end-users some guidance on model selection and expected accuracy. Moreover, this study addresses the need to systematically explore the errors in both the simulations and experiments, as well as to develop data-driven surrogate models [35] with the support of more simulation and experimental results.

Acknowledgments

Wentao Yan was a postdoctoral fellow at Northwestern University and a guest researcher at NIST under the support of the Cooperative Agreement

(70NANB17H283) when the authors started the work, and he continued this work in Singapore under the financial support of Singapore Ministry of Education Academic Research Fund Tier 1. Gregory Wagner and Wing Kam Liu would like to acknowledge the support by the National Science Foundation (NSF) Cyber-Physical Systems (CPS) under grant No. CPS/CMMI-1646592. The isotherm migration calculation was based on Dr. F Lopez's previous work at NIST after minor modifications. The authors are thankful to the discussion with Dr. Brandon Lane, Dr. Ho Yeung, Dr. Jarred Heigel and several other colleagues at NIST.

References

[1] L. Yang, O. Harrysson, H. West, D. Cormier, Compressive properties of Ti–6Al–4V auxetic mesh structures made by electron beam melting, Acta Materialia 60 (2012) 3370–3379.

[2] W. Ge, F. Lin, C. Guo, Microstructure and mechanical property of electron beam selective melting Ti-6Al-4V/TiAl structural gradient material, in: 26th Annual International Symposium on Solid Freeform Fabrication, Austin, Texas.

[3] W. Ge, C. Guo, F. Lin, Microstructures of components synthesized via electron beam selective melting using blended pre-alloyed powders of Ti-6Al-4V and Ti-45Al-7Nb, Rare Metal Materials and Engineering 44 (2015) 2623–2627.

[4] C. Guo, W. Ge, F. Lin, Dual-material electron beam selective melting: Hardware development and validation studies, Engineering 1 (2015) 124.

[5] C. Körner, A. Bauereiß, E. Attar, Fundamental consolidation mechanisms during selective beam melting of powders, Modelling and Simulation in Materials Science and Engineering 21 (2013) 085011.

[6] S. A. Khairallah, A. T. Anderson, A. Rubenchik, W. E. King, Laser powder-bed fusion additive manufacturing: Physics of complex melt flow and formation mechanisms of pores, spatter, and denudation zones, Acta Materialia 108 (2016) 36–45.

[7] W. King, A. Anderson, R. Ferencz, N. Hodge, C. Kamath, S. Khairallah, Overview of modelling and simulation of metal powder bed fusion

process at lawrence livermore national laboratory, Materials Science and Technology 31 (2015) 957–968.

[8] C. Qiu, C. Panwisawas, M. Ward, H. C. Basoalto, J. W. Brooks, M. M. Attallah, On the role of melt flow into the surface structure and porosity development during selective laser melting, Acta Materialia 96 (2015) 72–79.

[9] W. Yan, W. Ge, Y. Qian, S. Lin, B. Zhou, W. K. Liu, F. Lin, G. J. Wagner, Multi-physics modeling of single/multiple-track defect mechanisms in electron beam selective melting, Acta Materialia 134 (2017) 324–333.

[10] W. Yan, Y. Qian, W. Ge, S. Lin, W. K. Liu, F. Lin, G. J. Wagner, Meso-scale modeling of multiple-layer fabrication process in selective electron beam melting: inter-layer/track voids formation, Materials & Design 141 (2018) 210–219.

[11] M. Bayat, S. Mohanty, J. H. Hattel, A systematic investigation of the effects of process parameters on heat and fluid flow and metallurgical conditions during laser-based powder bed fusion of ti6al4v alloy, International Journal of Heat and Mass Transfer 139 (2019) 213–230.

[12] W. Yan, J. Smith, W. Ge, F. Lin, W. K. Liu, Multiscale modeling of electron beam and substrate interaction: a new heat source model, Computational Mechanics 56 (2015) 265–276.

[13] W. Yan, W. Ge, J. Smith, S. Lin, O. L. Kafka, F. Lin, W. K. Liu, Multi-scale modeling of electron beam melting of functionally graded materials, Acta Materialia 115 (2016) 403–412.

[14] W. Yan, W. Ge, J. Smith, G. Wagner, F. Lin, W. K. Liu, Towards high-quality selective beam melting technologies: Modeling and experiments of single track formations, in: 26th Annual International Symposium on Solid Freeform Fabrication, Austin, Texas.

[15] W. Yan, S. Lin, O. L. Kafka, Y. Lian, C. Yu, Z. Liu, J. Yan, S. Wolff, H. Wu, E. Ndip-Agbor, M. Mozaffar, K. Ehmann, J. Cao, G. J. Wagner, W. K. Liu, Data-driven multi-scale multi-physics models to derive process–structure–property relationships for additive manufacturing, Computational Mechanics 61 (2018) 521–541.

[16] W. Devesse, D. De Baere, P. Guillaume, The isotherm migration method in spherical coordinates with a moving heat source, International Journal of Heat and Mass Transfer 75 (2014) 726–735.

[17] F. Lopez, P. Witherell, B. Lane, Identifying uncertainty in laser powder bed fusion models, in: ASME 2016 11th International Manufacturing Science and Engineering Conference, American Society of Mechanical Engineers, pp. V003T08A005–V003T08A005.

[18] T. Moges, P. Witherell, G. Ameta, On characterizing uncertainty sources in laser powder bed fusion additive manufacturing models, in: ASME International Mechanical Engineering Congress and Exposition, volume 59377, American Society of Mechanical Engineers, p. V02AT02A061.

[19] T. Moges, W. Yan, S. Lin, G. Ameta, J. Fox, P. Witherell, Quantifying uncertainty in laser powder bed fusion additive manufacturing models and simulations, in: Solid Freeform Fabrication Symposium An Additive Manufacturing Conference.

[20] G. Tapia, W. King, L. Johnson, R. Arroyave, I. Karaman, A. Elwany, Uncertainty propagation analysis of computational models in laser powder bed fusion additive manufacturing using polynomial chaos expansions, Journal of Manufacturing Science and Engineering 140 (2018).

[21] W. Ge, W. Yan, S. Han, S. J. Na, Numerical modelling of surface morphology in selective laser melting, under review (2019).

[22] J. Smith, W. Xiong, W. Yan, S. Lin, P. Cheng, O. L. Kafka, G. J. Wagner, J. Cao, W. K. Liu, Linking process, structure, property, and performance for metal-based additive manufacturing: computational approaches with experimental support, Computational Mechanics 57 (2016) 583–610.

[23] J. Smith, W. Xiong, J. Cao, W. K. Liu, Thermodynamically consistent microstructure prediction of additively manufactured materials, Computational Mechanics 57 (2016) 359–370.

[24] Aerospace Specification Metals Inc., Special metals inconel alloy 625, http://asm.matweb.com/search/SpecificMaterial.asp?bassnum=NINC33, 2013. Accessed: 2018-10-10.

[25] Special Metals Corporation, Inconel alloy 625, http://www.specialmetals.com/assets/smc/documents/alloys/inconel/inconel-alloy-625.pdf, 2013. Accessed: 2018-10-10.

[26] Z. Taha-Al, M. Hashmi, B. Yilbas, Laser treatment of hvof coating: model study and characterization, Journal of mechanical science and technology 21 (2007) 1439.

[27] S. M. H. Hojjatzadeh, N. D. Parab, W. Yan, Q. Guo, L. Xiong, C. Zhao, L. I. Escano, M. Qu, X. Xiao, K. Fezzaa, W. Everhart, T. Sun, L. Chen, Mechanisms of pore elimination during 3d printing of metals, Nature Communications 10 (2019) 3088.

[28] S. Grantham, B. Lane, J. Neira, S. Mekhontsev, M. Vlasea, L. Hanssen, Optical design and initial results from nist's ammt/temps facility, in: Laser 3D Manufacturing III, volume 9738, International Society for Optics and Photonics, p. 97380S.

[29] J. C. Fox, B. M. Lane, H. Yeung, Measurement of process dynamics through coaxially aligned high speed near-infrared imaging in laser powder bed fusion additive manufacturing, in: Thermosense: Thermal Infrared Applications XXXIX, volume 10214, International Society for Optics and Photonics, p. 1021407.

[30] A. Kamara, W. Wang, S. Marimuthu, L. Li, Modelling of the melt pool geometry in the laser deposition of nickel alloys using the anisotropic enhanced thermal conductivity approach, Proceedings of the Institution of Mechanical Engineers, Part B: Journal of Engineering Manufacture 225 (2011) 87–99.

[31] S. Zhang, B. Lane, J. Whiting, K. Chou, On thermal properties of metallic powder in laser powder bed fusion additive manufacturing, Journal of Manufacturing Processes 47 (2019) 382–392.

[32] A. Klassen, V. E. Forster, C. Körner, A multi-component evaporation model for beam melting processes, Modelling and Simulation in Materials Science and Engineering 25 (2016) 025003.

[33] R. Cunningham, C. Zhao, N. Parab, C. Kantzos, J. Pauza, K. Fezzaa, T. Sun, A. D. Rollett, Keyhole threshold and morphology in laser

melting revealed by ultrahigh-speed x-ray imaging, Science 363 (2019) 849–852.

[34] R. Sibson, A brief description of natural neighbour interpolation, Interpreting multivariate data (1981).

[35] J. Li, R. Jin, Z. Y. Hang, Integration of physically-based and data-driven approaches for thermal field prediction in additive manufacturing, Materials & Design 139 (2018) 473–485.